

Deformation of a sheared magnetic droplet in a viscous fluid

Wellington C. Jesus^{1,*}, Alexandre M. Roma¹, and Hector D. Ceniceros²

¹ *Departamento de Matemática Aplicada, Universidade de São Paulo, Caixa Postal 66281, CEP 05311-970, São Paulo-SP, Brasil.*

² *Department of Mathematics, University of California, Santa Barbara, California, 93106 United States of America.*

Abstract. A fully three-dimensional numerical study of the dynamics and field-induced deformation of a sheared, superparamagnetic ferrofluid droplet immersed in a Newtonian viscous fluid is presented. The system is a three-dimensional, periodic channel with top and bottom walls displaced to produce a constant shear rate and with an external, uniform magnetic field perpendicular to the walls. The model consists of the incompressible Navier-Stokes equations with the extra magnetic stress coupled to the static Maxwell's equations. The coupled system is solved with unprecedented resolution and accuracy using a fully adaptive, Immersed Boundary Method. For small droplet distortions, the numerical results are compared and validated with an asymptotic theory. For moderate and strong applied fields, relative to surface tension, and weak flows a large field-induced droplet deformation is observed. Moreover, it is found that the droplet distortion in the vorticity direction can be of the same order as that occurring in the shear plane. This study highlights the importance of the three-dimensional character of a problem of significant relevance to applications, where a dispersed magnetic phase is employed to control the rheology of the system.

AMS subject classifications: 65Z05, 65M55, 65M06, 65M99, 76D99

Key words: drop, ferrofluid, front-tracking method, shear flow.

1 Introduction

Magnetic fluids, also known as *ferrofluids*, are synthetic suspensions composed of solid magnetic particles coated with a surfactant and suspended in a liquid carrier. In general, particles are of magnetite with a diameter on the order of 3 nm to 15 nm (nanoparticles) and the liquid carrier is typically oil or water (a Newtonian fluid). Thermal agitation

*Corresponding author. *Email addresses:* wcjesus@ime.usp.br (W. C. Jesus), roma@ime.usp.br (A. M. Roma), hdc@math.ucsb.edu (H. D. Ceniceros)

keeps particles suspended due to Brownian motion while a surfactant (or electrically charged particles) prevents them from clustering together [1–3].

An applied magnetic field, even of moderate intensity, can dramatically change the rheology of a ferrofluid. This is significant for a number of applications in which the magnetic component phase is used for controlling the system. In particular, two-phase systems consisting of ferrofluid droplets immersed in a Newtonian carrier have a great potential in important technological applications such as in the design of new, functional materials [4] and in the delivery of drugs [5, p. 233] [6–8].

Several numerical investigations have been devoted to the deformation of ferrofluid droplets under different flow and field conditions. Most studies have been either two-dimensional or axi-symmetric [9–15]. Interface instabilities of a ferrofluid droplet under the influence of an imposed magnetic field have also received considerable attention [16–18].

In this work, we focus on the field-induced distortion of a ferrofluid droplet in shear flow. We are inspired by the work of [14] on such deformation in quiescent flow. To this end, we perform fully three-dimensional numerical simulations employing an adaptive Immersed Boundary Method. This is coupled to an efficient, adaptive finite difference solver for the static Maxwell’s equations to obtain the magnetic field. The building blocks of this methodology, introduced in different contexts [1, 19, 20], are here combined and applied for the first time for fully three-dimensional ferrofluid simulations. The mesh adaptive methodology allow us to compute the flow and the droplet deformation with unprecedented resolution and accuracy. However, our simulations are limited to small capillary numbers (see Section 2.2 for a description of all dimensionless groups) and we consider only a small number of points in parameter space due to the enormous computational cost for each simulation to steady state (weeks of CPU and some of them months). Nevertheless, our study shows clearly the significant field-induced distortions of the ferrofluid droplet and the effect of the field on the direction of maximal deformation and on the overall dynamics towards steady state. In particular, we find that for moderate to strong fields (relative to surface tension) and weak flows, the field-induced droplet distortion can be quite significant. Moreover, the droplet deformation in the vorticity direction can be of the same order as that occurring in the shear plane. This and other results in this study highlight the importance of the three-dimensional character of this significant rheological problem.

The paper is organized as follows: In Section 2, we present the governing equations, the immersed boundary formulation, and the nondimensional form of the equations. The physical parameters used in this study, which correspond to an actual PDMS ferrofluid droplet suspended in viscous medium, are given at the end of this section. We summarize the numerical methodology in Section 3. More details of the numerical discretization appear in Appendix A. Section 4 is devoted to the numerical results, including a validation and a comparison with an asymptotic small deformation theory. Considerations about a verification of the numerical accuracy are presented in Appendix B. A resolution study and an investigation of domain size effects are outlined in Appendix C. Some

concluding remarks are given in Section 5.

2 Governing equations

We consider a three-dimensional rectangular channel Ω filled with a Newtonian fluid in which there is a suspended, neutrally buoyant, ferrofluid drop. $S(t)$ is the separation interface, $\Omega_d(t)$ and $\Omega_c(t)$ are the regions inside and outside of the drop, respectively (“d” stands for *disperse* phase (the drop) and “c” for *continuous* phase - the surrounding fluid). The system is subjected to a simple shear arising by moving the top and bottom walls with constant relative velocity. The two fluid components are assumed to be incompressible, immiscible, and density matched.

Macroscopically, the system is described by the conservation of linear momentum and by the incompressibility constraint

$$\rho \frac{D\mathbf{u}}{Dt} = -\nabla p + \nabla \cdot (2\eta \mathbf{E}) + \nabla \cdot \boldsymbol{\tau}_m + \mathbf{f}_s, \quad (2.1)$$

$$\nabla \cdot \mathbf{u} = 0, \quad (2.2)$$

where D/Dt is the material derivative, \mathbf{u} is the velocity field, p is the pressure, ρ is the specific mass, and η is the (kinematic) viscosity. In (2.1), $\mathbf{E} = (\nabla \mathbf{u} + \nabla \mathbf{u}^T)/2$ is the deformation tensor (rate of strain) and $\boldsymbol{\tau}_m$ is the stress stemming from the magnetic nanoparticles, coupling the nano-structure with the macroscopic flow. The term \mathbf{f}_s is the interfacial tension force.

The material properties ρ and η are constant within each phase but will vary in time and space due to the drop motion, that is,

$$\eta = \begin{cases} \eta_d & \text{in } \Omega_d(t), \\ \eta_c & \text{in } \Omega_c(t), \end{cases} \quad (2.3)$$

and similarly for ρ .

An imposed external magnetic field \mathbf{H}_0 interacts with the magnetic particles in the ferrofluid drop affecting its magnetization. There are no free currents in either region so the magnetic induction \mathbf{B} and the magnetic field \mathbf{H} of the system satisfy the magnetostatic Maxwell equations [1]

$$\nabla \cdot \mathbf{B} = 0 \quad \text{and} \quad \nabla \times \mathbf{H} = 0 \quad \text{in } \Omega, \quad (2.4)$$

and

$$\mathbf{B} = \begin{cases} \mu_0(\mathbf{H} + \mathbf{M}) & \text{in } \Omega_d(t), \\ \mu_0 \mathbf{H} & \text{in } \Omega_c(t), \end{cases} \quad (2.5)$$

where μ_0 is the permeability constant of vacuum. We consider a linearly magnetizable ferrofluid. In that context, for sufficiently small magnetic particles ($\lesssim 6 \text{ nm}$ in diameter)

the magnetization becomes aligned almost instantly with the magnetic field, that is $\mathbf{M} = \chi \mathbf{H}$, where χ is the magnetic susceptibility. If we assume the *superparamagnetic* behavior, that is, $\mathbf{B} = \mu_0(1 + \chi) \mathbf{H}$, and use the fact that there is a scalar potential ψ (since $\nabla \times \mathbf{H} = 0$) satisfying $\mathbf{H} = \nabla \psi$, it follows that

$$\nabla \cdot (\mu \nabla \psi) = 0 \quad \text{in } \Omega \quad \text{and} \quad \frac{\partial \psi}{\partial n} \Big|_{\partial \Omega} = \mathbf{n} \cdot \mathbf{H}_0, \quad (2.6)$$

where

$$\mu = \begin{cases} \mu_0(1 + \chi) & \text{in } \Omega_d(t) \\ \mu_0 & \text{in } \Omega_c(t). \end{cases} \quad (2.7)$$

For a superparamagnetic ferrofluid, the magnetic force density is given by [1] $\nabla \cdot (\mu \mathbf{H} \otimes \mathbf{H}) - (1/2) \mu_0 \nabla \mathbf{H} \cdot \mathbf{H}$, the last term being proportional to the identity matrix and, at the momentum equation (2.1), it may be merged into the pressure field on the entire domain. In that context, we may take the magnetic stress as being

$$\boldsymbol{\tau}_m = \mu \mathbf{H} \otimes \mathbf{H}, \quad (2.8)$$

thus the magnetic force is computed by

$$\mathbf{f}_m = \nabla \cdot \boldsymbol{\tau}_m. \quad (2.9)$$

2.1 Free boundary problem

The problem under consideration is a *free boundary problem* in the sense that the drop surface $S(t)$ has to be computed simultaneously with the other unknowns. Here, the interface $S(t)$ is represented by a parametric form $\mathbf{X}(\boldsymbol{\alpha}, t) = (X(\boldsymbol{\alpha}, t), Y(\boldsymbol{\alpha}, t), Z(\boldsymbol{\alpha}, t))$, with $\boldsymbol{\alpha} = (\alpha_1, \alpha_2)$ the *Lagrangian parameter*, such that

$$S = S(t) = \{\mathbf{X}(\boldsymbol{\alpha}, t) \mid \boldsymbol{\alpha} \in \Sigma_0\}, \quad (2.10)$$

where Σ_0 is a fixed domain. As in [19] and in [20], the interface is treated as an “immersed boundary” that moves with local fluid velocity

$$\frac{\mathbf{X}(\boldsymbol{\alpha}, t)}{\partial t} = \mathbf{U}(\boldsymbol{\alpha}, t) \doteq \mathbf{u}(\mathbf{X}(\boldsymbol{\alpha}, t), t) = \int_{\Omega} \mathbf{u}(\mathbf{x}, t) \delta(\mathbf{x} - \mathbf{X}(\boldsymbol{\alpha}, t)) d\mathbf{x}, \quad (2.11)$$

and exerts the interfacial force

$$\mathbf{F}(\boldsymbol{\alpha}, t) = \kappa \sigma \mathbf{n} \quad (2.12)$$

on the fluid, where \mathbf{x} represents the Eulerian spatial position, $\delta(\cdot)$ is the usual three-dimensional Dirac delta function used in the *immersed boundary method* [19, 21, 22], κ is the curvature of the interface, σ is the interfacial tension coefficient, and \mathbf{n} is the unit exterior

normal vector to interface S . The force \mathbf{F} , defined solely on S , balances the normal stress jump between the two fluid phases and it is used to compute the interfacial tension force applied to the fluid which is given by

$$\mathbf{f}_s(\mathbf{x}, t) = \int_S \mathbf{F}(\boldsymbol{\alpha}, t) \delta(\mathbf{x} - \mathbf{X}(\boldsymbol{\alpha}, t)) dS, \mathbf{x} \in \Omega. \quad (2.13)$$

We note that the velocity is continuous across the free surface S .

The discrete version of relations (2.11)-(2.13), in which the δ distribution is replaced by a function of finite support, are known as the *interpolation* and *spreading* operators in the Immersed Boundary Method.

2.2 Non-dimensional equations, dimensionless groups

We select as characteristic length and time scales the radius a of the initially undeformed drop and the inverse of the shear rate, $1/\dot{\gamma}$, respectively. The pressure is scaled by $\eta_c \dot{\gamma}$, the magnetic permeability by μ_0 , and the magnetic field by H_0 (the intensity of the applied field).

The non-dimensional equations of motion are:

$$Re \left(\rho \frac{D\mathbf{u}}{Dt} \right) = -\nabla p + \nabla \cdot (2\eta \mathbf{E}) + 2 \frac{Bo_m}{Ca} \nabla \cdot \boldsymbol{\tau}_m + \frac{1}{Ca} \mathbf{f}_s, \quad (2.14)$$

$$\nabla \cdot \mathbf{u} = 0, \quad (2.15)$$

where the dimensionless groups are

$$Re = \frac{\rho_c a^2 \dot{\gamma}}{\eta_c}, \quad (2.16)$$

$$Ca = \frac{\eta_c a \dot{\gamma}}{\sigma}, \quad (2.17)$$

$$Bo_m = \frac{a \mu_0 H_0^2}{2\sigma}, \quad (2.18)$$

the Reynolds number, the capillary number, and the magnetic Bond number, respectively. The ratio $M_n = Ca/Bo_m$ is called the Mason number.

Other important dimensionless parameters in the problem under consideration are

$$\lambda = \frac{\eta_d}{\eta_c}, \quad (2.19)$$

$$r_\mu = \frac{\mu_d}{\mu_0}, \quad (2.20)$$

the viscosity ratio, and the permeability ratio between the droplet and the surrounding fluid, respectively. For all the simulations we report on we take $\lambda = 1.5$ (for $Re = 0.549$) or $\lambda = 0.08$ (for $Re = 1.667 \times 10^{-5}$), the density of the ferrofluid drop is matched with the surrounding liquid so in this case the buoyancy is not considered in this study, and $r_\mu = (1 + \chi)$ with $\chi = 0.8903$.

2.3 The physical parameters

The underlying values of the physical parameters we used in the simulations are based on the ferrofluid droplet experiments by [14]. Namely, $a = 1.291 \times 10^{-3} m$, $\sigma = 1.35 \times 10^{-2} N \cdot m^{-1}$, $\eta_c = 0.1 N \cdot s \cdot m^{-2}$, $\eta_d = 0.15 N \cdot s \cdot m^{-2}$, $\mu_0 = 1.2566 \times 10^{-6} N \cdot A^{-2}$, and $\rho_c = 1.26 \times 10^3 kg \cdot m^{-3}$.

3 Numerical methodology

We take the computational domain to be the cube centered at the origin and of size $40a$, where a is the radius of the initial, spherical droplet. The size of the domain was selected through a numerical study to ascertain domain size effects, as documented in Appendix C. It was found that the difference between the drop deformation in this domain and in one twice as large was less than 0.14%. This domain is discretized with a structured, adaptive mesh refinement (AMR) technique [23,24] using six levels of refinement. The finest mesh (of mesh size $h = 0.0775a$) covers at all times the droplet and a neighborhood of it. As a comparison, a uniform mesh with this resolution would correspond to using 512^3 Eulerian mesh points.

To solve the flow equations (2.1)-(2.2), we employ the 3D AMR Immersed Boundary Method solver in [19]. This is based on a pressure-increment projection method with a second order, variable step semi-implicit discretization, and a *regular triangular mesh* [25] for the droplet surface. To prevent excessive Lagrangian node clustering on the free surface mesh, we apply a grid optimization that restrict vertices to slide slightly, while constrained to the surface, to conveniently adjust their positions (see [19] for more details). These Lagrangian mesh operations are handled with the aid of the free, open-source software GTS - the GNU Triangulated Surface Library (<http://gts.sourceforge.net>).

The aforementioned flow solver has been thoroughly tested [19,20] and been found to exhibit second order accuracy for smooth velocity fields. In the present work, we add to this efficient fluid solver an AMR, second order method for the magnetic potential equation (2.6). The discretization of this equation as well as that of the term $\nabla \cdot \boldsymbol{\tau}_m$ are detailed in Appendix A.

4 Numerical results

The computational domain is the cubic channel $[-C, C] \times [-C, C] \times [-C, C]$, where $C = 20a$. The top and bottom domain's faces are considered to be solid walls (no-slip velocity boundary condition) while periodic boundary conditions are applied at the other faces. An initially spherical, ferrofluid droplet of radius a is placed at the origin. The ratio of the droplet viscosity to the surrounding, Newtonian fluid viscosity is $\lambda = 1.5$ and the magnetic susceptibility is $\chi = 0.8903$. These two parameters remain fixed for all the simulations. When applied, the external magnetic field \mathbf{H}_0 ($B_{0m} > 0$), is uniform and in the

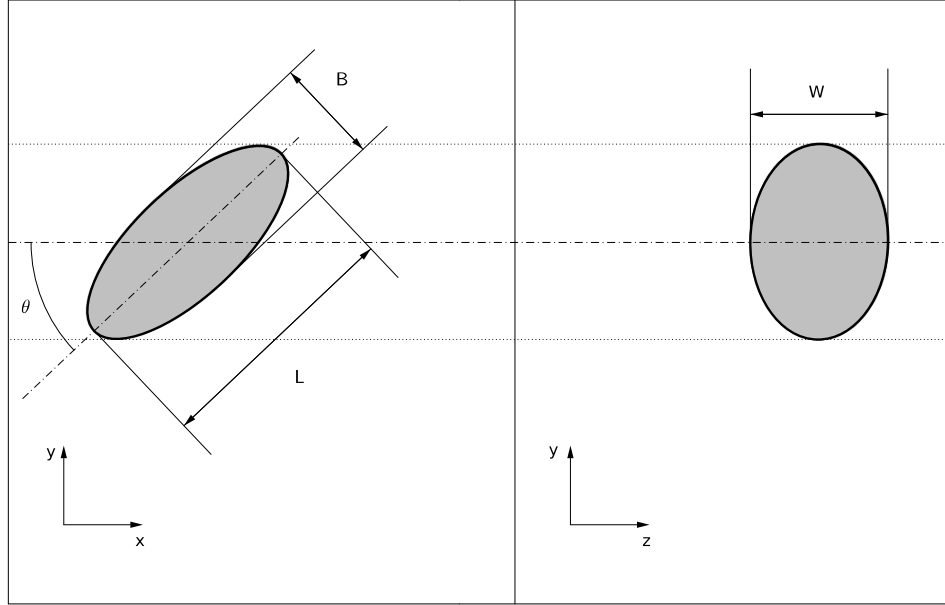


Figure 1: L and B are the length of the major and minor principal axes of the droplet elliptical cross section cut by the shear plane (left). The orientation angle θ is defined with respect to the x (flow) axis. W is the extent of the droplet in the z (vorticity) direction, as defined by the elliptical cross section cut by the velocity gradient-vorticity plane (right).

normal-wall (y) direction.

As a validation test, we consider first the deformation of a ferrofluid droplet under an applied magnetic field in quiescent flow. After that, we exclusively focus on the magnetic field-induced droplet deformation under simple shear flow for small Ca . To produce this flow with a constant shear rate $\dot{\gamma}$, we move the domain's top and bottom walls with a constant velocity difference of $2C\dot{\gamma}$. For future reference in the shear flow results, we call x the streamwise direction, y the velocity gradient direction, and z the vorticity direction.

In this work we focus on small Ca cases to accurately resolve the drop distortion in 3D and to better quantify the effect on an applied magnetic field. We emphasize that all the numerical simulations we report on are fully three-dimensional. We do not assume any symmetries of the numerical solution.

4.1 Validation in quiescent flow

If the steady state shape of a *superparamagnetic*, ferrofluid droplet under imposed uniform magnetic field \mathbf{H}_0 is a prolate ellipsoid (i.e. $B=W < L$ in Figure 1), the problem is similar to that of a dielectric ellipsoid in a uniform external electrical field, as pointed out by [14]. In this situation, the intensity of the field inside the droplet is constant and is given by [14,26,

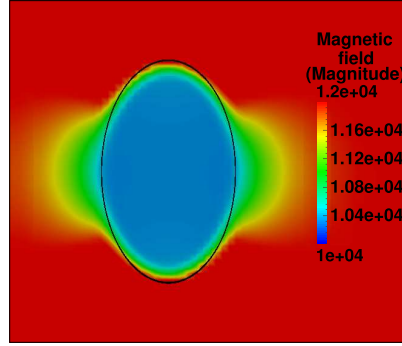


Figure 2: Planar, xy cross section of the magnetic field magnitude ($A \cdot m^{-1}$) in the interior and a vicinity of a ferrofluid drop in its steady state, obtained from a full 3D simulation with $Bo_m = 4.4475$, $\lambda = 1.5$ and $\chi = 0.8903$.

p. 42]

$$H_{theory} = \frac{\mu_c H_0}{(1-\nu)\mu_c + \nu\mu_d}, \quad (4.1)$$

where μ_c and μ_d are the magnetic permeability of the *continuous* and *dispersed* phases, respectively, ν is the demagnetization factor

$$\nu = \left(\frac{1-E^2}{2E^3} \right) \left(\ln \frac{1+E}{1-E} - 2E \right),$$

with eccentricity $E = \sqrt{1-B^2/L^2}$. L and B are the length of the ellipsoid principal axes (Figure 1, L is aligned to the direction of the imposed magnetic field \mathbf{H}_0).

Starting from a quiescent flow, we perform a fully 3D simulation, up to steady state, of an initially spherical ferrofluid droplet immersed in a Newtonian fluid and subjected to a uniform magnetic field. We use the same physical parameters that [14] employed in their experiments (see end of Section 2.2, $H_0 = 1.2167 \times 10^4 A \cdot m^{-1}$). Figure 2 displays a cross section of the magnetic field magnitude inside the droplet at steady state. Away from the droplet surface, the magnetic field is approximately constant; it ranges between 1.01×10^4 and $1.04 \times 10^4 A \cdot m^{-1}$ and it is within 1.54% of the theoretical value $H_{theory} = 1.0240 \times 10^4 A \cdot m^{-1}$. Near the droplet surface there are larger deviations from H_{theory} , partly due to the spreading of the magnetic force by the Immersed Boundary Method. The full 3D simulation gives a droplet with $B/W = 1.000033419$ and $B/L = 0.604$, i.e. a prolate shape up to 4 digits of accuracy.

4.2 Comparison with small deformation theory: small Ca and Bo_m

The deformation and dynamics of a Newtonian drop in a viscous fluid undergoing a shear flow, and with negligible inertia ($Re \approx 0$), are well understood [27,28]. The straining

component of the flow promotes the drop's deformation while surface tension acts as a restoring force. The capillary number Ca represents the ratio of these competing forces. The deformation is also dependent on the viscosity ratio λ of the drop and the suspending fluid. To quantify drop distortions of small to moderate size Taylor's deformation parameter

$$D = \frac{L-B}{L+B}, \quad (4.2)$$

with L and B as defined in Figure 1, is usually employed. However, D does not offer information of the deformation in the vorticity direction (the length W defined in Figure 1). For small Ca , i.e. surface tension dominating flow forces, there is small deformation, D is linear with Ca , and the viscosity ratio λ has only a weak effect [29]. For $Ca > O(1)$ there is substantial deformation unless, λ is very large, in which case the drop spins like a rigid body motion if the local vorticity is strong enough. Finally, if $\lambda \ll 1$ and $Ca \gg 1$, pointed and highly elongated thin drop shapes can form [27, 28]. The direction of maximal distortion varies with Ca and with time [27]. For $Ca \ll 1$, the angle θ of the direction of maximum drop extension relative to the x axis approaches $\pi/4$, which is the shear flow's direction of principal extension. However, the equilibrium value of θ is not approached monotonically; there are oscillations which are eventually damped out by surface tension and viscous dissipation.

For a Newtonian drop in Stokes flow, there is a small deformation ($Ca \ll 1$) theory originated with Taylor's work [29]. The idea is to do perturbation analysis in the small deviations from the spherical shape using the exact Stokes flow solution of the latter. This analysis can be directly extended to a slightly deformed sheared, ferrofluid droplet with an applied field in the limit of both small Ca and small Bo_m , as we outline next.

Assuming the normal-stress balance has a magnetic contribution component and a curvature variation proportional to $O(Ca^2)$, $O(CaBo_m)$, and $O(Bo_m^2)$, the equation for the perturbed droplet radius r_s may be written as

$$r_s = 1 + \alpha(\lambda)Ca \mathbf{x} \cdot \mathbf{E} \cdot \mathbf{x} + \beta(\chi)Bo_m \mathbf{x} \cdot \mathbf{A} \cdot \mathbf{x}, \quad (4.3)$$

where \mathbf{E} is the rate-of-strain tensor and \mathbf{A} is the irreducible (traceless) form of Maxwell's magnetic tensor (both tensors in dimensionless form). Following the steps detailed in [30] and using the analytical solution of the magnetic field for a non-conducting sphere in a uniform field in [26, p. 42] and [31, p. 364], we obtain

$$\alpha(\lambda) = \frac{19\lambda + 16}{8(\lambda + 1)}, \quad (4.4)$$

$$\beta(\chi) = \frac{3\chi(2\chi + 1)}{4(\chi + 3)^2}. \quad (4.5)$$

It is important to note, however, that the normal stress balance cannot be satisfied at all the surface points [14, 32, 33]. Here, we opted to enforce it on the six intersection points of the coordinate axes with the sphere, assuming that $Ca \ll 1$ and $Bo_m \ll 1$.

The deformation along the principal axes and the direction of maximal deformation can now be estimated from the eigenvalues of $(\alpha\mathbf{E} + \beta\mathbf{A})$ to yield:

$$L/(2a) \approx 1 + \frac{1}{6}\beta(\chi)Bo_m + \frac{1}{2}\sqrt{[\alpha(\lambda)Ca]^2 + [\beta(\chi)Bo_m]^2}, \quad (4.6)$$

$$B/(2a) \approx 1 + \frac{1}{6}\beta(\chi)Bo_m - \frac{1}{2}\sqrt{[\alpha(\lambda)Ca]^2 + [\beta(\chi)Bo_m]^2}, \quad (4.7)$$

$$W/(2a) \approx 1 - \frac{1}{3}\beta(\chi)Bo_m, \quad (4.8)$$

and hence

$$D \approx \frac{\sqrt{[\alpha(\lambda)Ca]^2 + [\beta(\chi)Bo_m]^2}}{2 + \frac{1}{3}\beta(\chi)Bo_m}. \quad (4.9)$$

Clearly, (4.9) reduces to Taylor's classical result in the limit $Bo_m \rightarrow 0$. It is important to note that for $Bo_m = 0$, $W/(2a) - 1 = O(Ca^2)$ [34, 35] and this is one of the reasons why the planar, Taylor deformation parameter D is usually employed as a measure of small drop distortion in Newtonian flows. But for $Bo_m > 0$, (4.8) shows that the field-induced variation in W , under the small deformation assumption, is $O(Bo_m)$ and hence the importance of three-dimensional computations.

To test this asymptotic formula we perform full 3D simulations for eight sets of small Bo_m and Ca , with $Bo_m = 2Ca$ (i.e. Mason number $M_n = 2$). This is done by varying the surface tension with $Re = 1.667 \times 10^{-5}$ or $Re = 0.549$. With this choice of M_n , the coefficient in the magnetic force term ($\nabla \cdot \boldsymbol{\tau}_m$) in the momentum equation (2.14) is 1. Note that since $\alpha(0.08) = 2.02778$ or $\alpha(1.5) = 2.2250$ and $\beta(0.8903) = 0.1227$, the asymptotic formula (4.9) predicts that the deformation due to the straining flow will dominate over the field-induced distortion for $Ca/Bo_m = 2$. Figures 3 and 4 offer a comparison of the numerical results for D and the asymptotic formula (4.9). There is good agreement for cases with $Re = 1.667 \times 10^{-5}$ (Figure 3) but the asymptotic prediction slightly underestimates the three computed values presented in Figure 4. The discrepancy could be attributed to small inertial effects present at $Re = 0.549$.

Tables 1 and 2 provides the relative (percentage) variation of the droplet principal axes, D , and θ . The changes in L and B (and therefore in D) are approximately linear in Bo_m , consistent with the asymptotic theory. However, this is evidently not the case for the variation of W , which approximately triples as Bo_m is doubled. Given that $\alpha(0.08) = 2.02778$ or $\alpha(1.5) = 2.2250$ and $\beta(0.8903) = 0.1227$, it is conceivable that the term of $O(Ca^2)$, which involves α as a factor in the $Bo_m = 0$ case [34], becomes commensurate with $\frac{1}{3}\beta(0.8903)Bo_m$ and this might explain the difference between the first order asymptotics (4.8) and the simulation results. It is also noteworthy that θ at steady state decreases as both Bo_m and Ca are increased but keeping their ratio fixed. This behavior for θ is typical for Newtonian drops under simple shear ([19], [36]) and in the current case is expected from the dominance of the flow strain over the magnetic force.

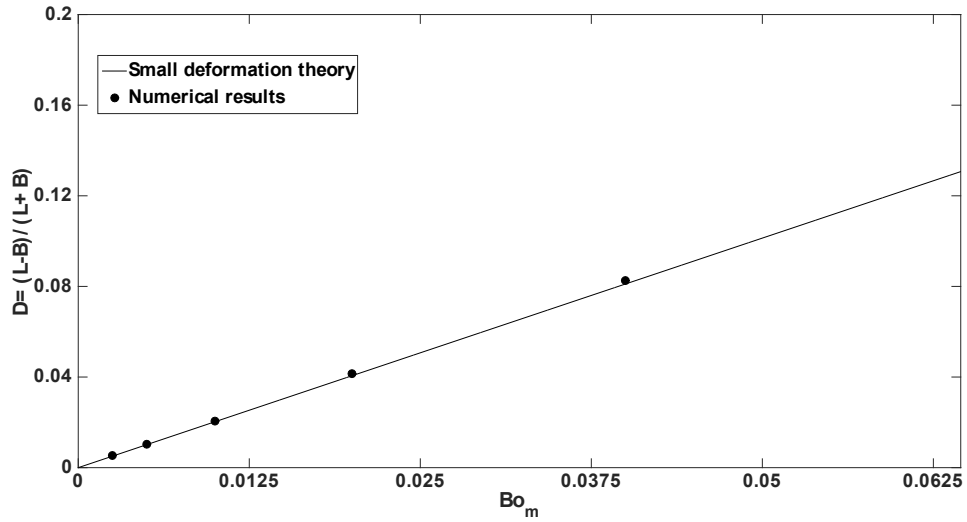


Figure 3: Comparison with the small deformation theory for $Bo_m = \frac{1}{2}Ca$. The numerical results correspond to the cases $Bo_m = 0.0025$, $Bo_m = 0.0050$, $Bo_m = 0.0100$, $Bo_m = 0.0200$ and $Bo_m = 0.0400$. $Re = 1.667 \times 10^{-5}$.

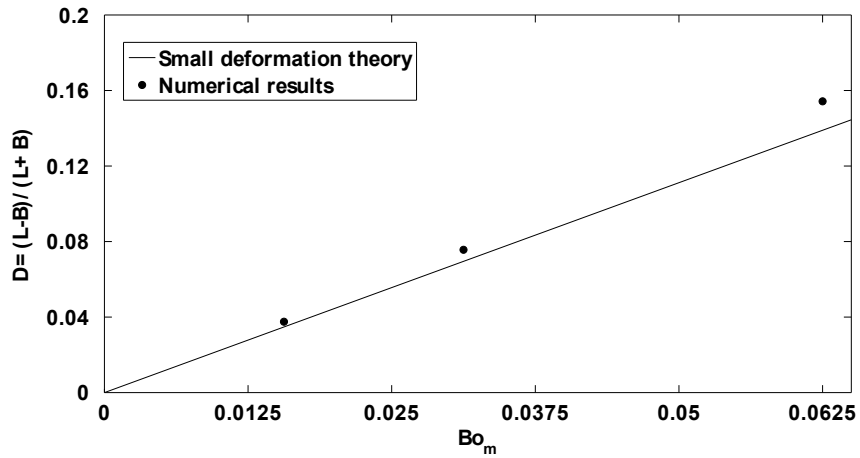


Figure 4: Comparison with the small deformation theory for $Bo_m = \frac{1}{2}Ca$. The numerical results correspond to the cases $Bo_m = 0.015625$, $Bo_m = 0.03125$ and $Bo_m = 0.0625$. $Re = 0.549$.

$Bo_m = \frac{1}{2}Ca$	$100\left(\frac{L-2a}{2a}\right)$	$100\left(\frac{B-2a}{2a}\right)$	$100\left(\frac{W-2a}{2a}\right)$	D	θ [rad]
2.5000×10^{-3}	0.534%	-0.513%	-0.029%	5.238×10^{-3}	0.78
5.0000×10^{-3}	1.067%	-1.024%	-0.044%	1.045×10^{-2}	0.74
1.0000×10^{-2}	2.134%	-1.968%	-0.086%	2.049×10^{-2}	0.74
2.0000×10^{-2}	4.354%	-3.956%	-0.219%	4.146×10^{-2}	0.73
4.0000×10^{-2}	9.006%	-7.648%	-0.660%	8.271×10^{-2}	0.70

Table 1: Relative changes of the length of the droplet principal axes, Taylor’s deformation parameter D , and the orientation angle θ at steady state. $Re = 1.667 \times 10^{-5}$.

$Bo_m = \frac{1}{2}Ca$	$100\left(\frac{L-2a}{2a}\right)$	$100\left(\frac{B-2a}{2a}\right)$	$100\left(\frac{W-2a}{2a}\right)$	D	θ [rad]
1.5625×10^{-2}	3.972%	-3.552%	-0.350%	3.754×10^{-2}	0.82
3.1250×10^{-2}	8.345%	-6.893%	-0.959%	7.564×10^{-2}	0.75
6.2500×10^{-2}	18.61%	-13.09%	-3.200%	1.543×10^{-1}	0.65

Table 2: Relative changes of the length of the droplet principal axes, Taylor’s deformation parameter D , and the orientation angle θ at steady state. $Re = 0.549$.

4.3 Sheared ferrofluid droplet deformation under a strong magnetic field

In this subsection we examine the influence of a strong applied field, relative to surface tension, on the distortion of a sheared droplet by comparing with the corresponding zero field case.

We take $Ca = 0.125$. Figure 5 shows the shape of the steady state droplet and the vorticity magnitude in a vicinity of the droplet for zero applied magnetic field ($Bo_m = 0$). There is strong vorticity concentrated around the regions of highest curvature.

We now look at the effects of a strong applied magnetic field, $H_0 = 1.2167 \times 10^4 \text{ A} \cdot \text{m}^{-1}$ ($Bo_m = 4.4475$), for the same $Ca = 0.125$. Figure 6 displays the steady state droplet shape, the magnetic field, and the vorticity magnitude in a neighborhood of the droplet. The vorticity is about twice as large and much more localized than that in the zero field case. The droplet deformation is substantial in both the shear plane and along the vorticity (z) direction. The magnetic field is largely uniform in the droplet interior and away from its surface, developing large gradients around the droplet tips in the external field direction.

To quantify the distortion of the sheared ferrofluid droplet with and without an applied magnetic field, we plot Taylor’s parameter D as a function of time in Figure 7(a). With the applied field, D reaches a steady state value of about 0.36, which is more than double that obtained in the absence of a field. The plots in Figure 8 containing the time

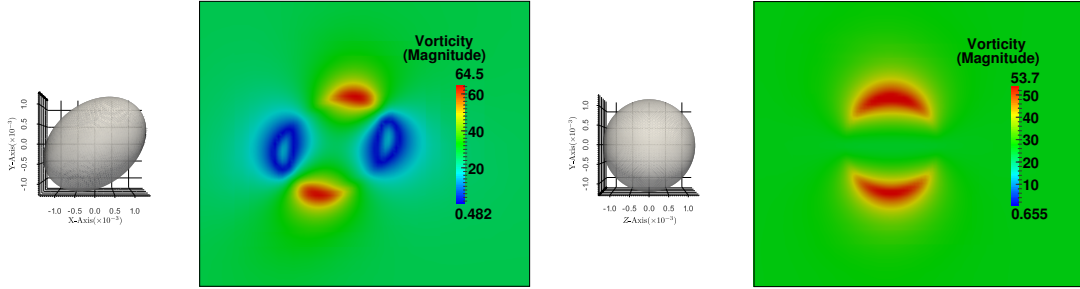


Figure 5: Steady state droplet shape and vorticity magnitude for zero external magnetic field, $Ca=0.125$, $Bo_m=0$, $Re=0.549$. Shear plane cross section (left) and velocity gradient-vorticity plane cross section (right).

evolution of the length of each of the droplet principal axes and the orientation angle, provide additional details of the droplet deformation and dynamics. First of all, even for $Bo_m=0$, the elongated droplet is not axisymmetric ($B \neq W$). Second, the field-induced variation of W , the droplet breadth in the vorticity direction, is about twice as much as that of B . These two observations underline the importance of full three-dimensional simulations. Finally, the plot of θ , the angle of droplet maximal extension direction, confirms the droplet wobbling motion toward a steady state and shows a marked shift toward the direction of the applied field ($\theta = \pi/2$).

We now halve Ca (by halving the shear rate $\dot{\gamma}$ and so Re is reduced accordingly) and examine again the effect of a strong applied field, $Bo_m = 4.4475$, by comparing with the zero-field, sheared droplet and with the previously discussed $Ca = 0.125$ case. As expected, the droplet is less deformed for the smaller value of Ca but as Figure 7(b) also demonstrates, the applied field produces a variation of D of about the same magnitude for both values of the capillary number. For these two weak flow situations, the magnetic force dominates over the straining flow and D is approximately proportional to Bo_m , as predicted by the asymptotic theory (4.9). Figure 9 provides the individual evolution of the droplet distortion along each of the principal axes and of the angle θ . When comparing with the $Ca = 0.125$ case (Figure 8), we observe that the most noticeable variations, relative to the zero-field case, occur in W and in θ . For the weaker flow, $Ca = 0.0625$, the main distortion is induced by the applied field. This is evident in the significant shift in θ to a value much closer to $\pi/2$ than to $\pi/4$.

4.4 Field-Induced droplet distortion for fixed Ca .

In our final study, we take $Ca=0.125$ fixed and consider three values of Bo_m , obtained by ten fold increases: $Bo_m=0.0625$, $Bo_m=0.625$, and $Bo_m=6.25$.

Table 3 presents the relative (percentage) changes of the droplet principal axes, D , and θ for these three very disparate magnetic Bond numbers. Despite the data being limited

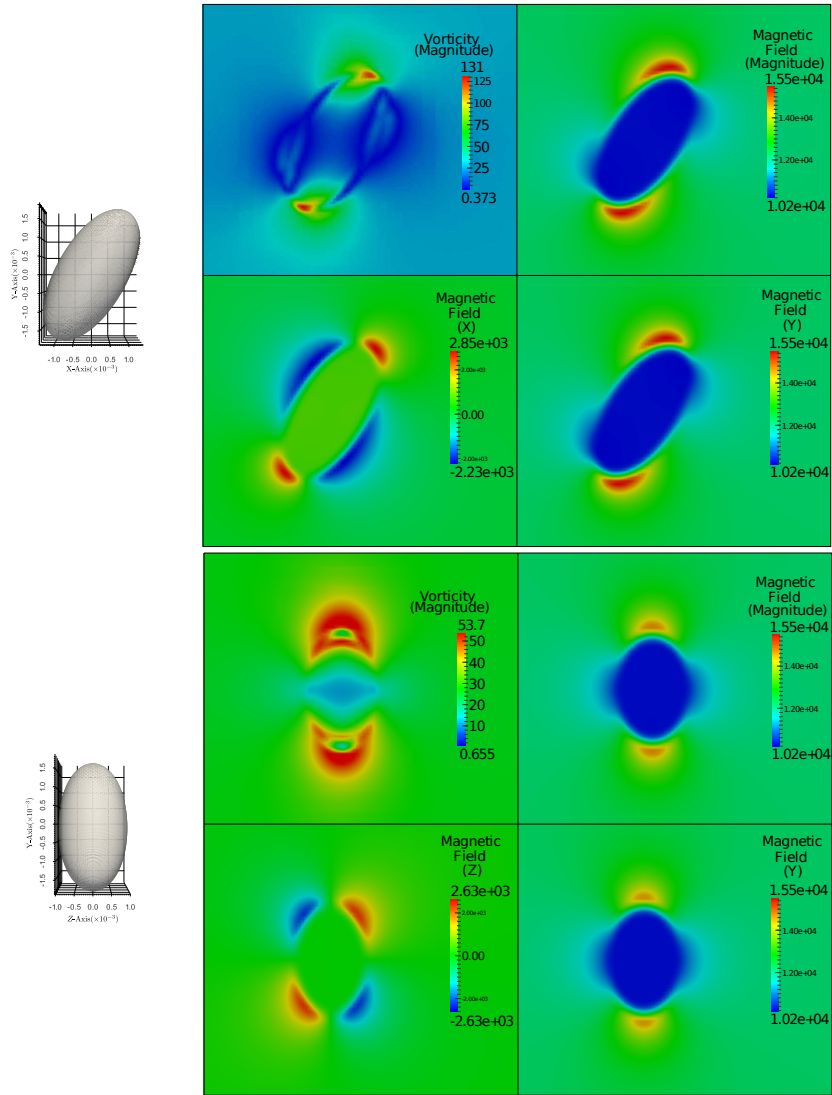


Figure 6: Steady state droplet, vorticity magnitude, and magnetic field ($A \cdot m^{-1}$) for $Bo_m = 4.4475$, $Ca = 0.125$, $Re = 0.549$. Upper plot: shear plane cross section. Lower plot: Velocity gradient-vorticity plane cross section.

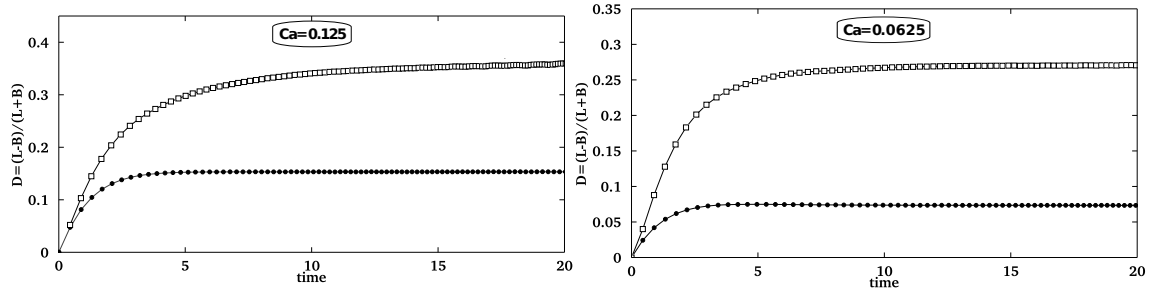


Figure 7: Time evolution of Taylor's deformation parameter D for (a) $Ca = 0.125$, $Re = 0.5490$ and (b) $Ca = 0.0625$, $Re = 0.2745$. The black circles correspond to the zero external field case ($Bo_m = 0$) and the unfilled squares to $Bo_m = 4.4475$.

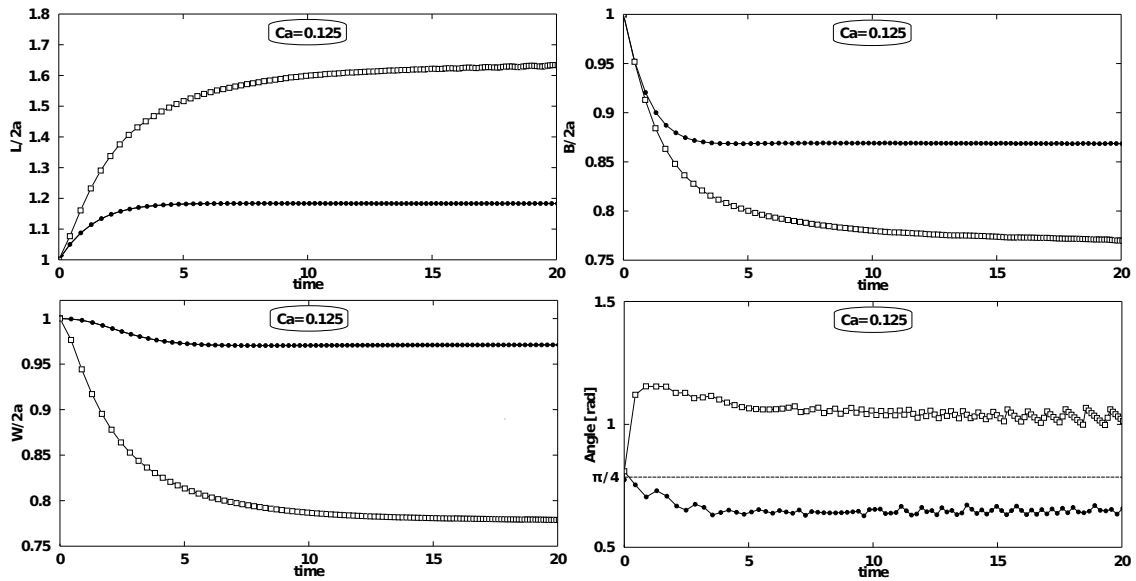


Figure 8: Time evolution of the (scaled) length of the droplet principal axes and the orientation angle for $Ca = 0.125$ and $Re = 0.549$. The black circles correspond to the zero external field case ($Bo_m = 0$) and the unfilled squares to $Bo_m = 4.4475$.

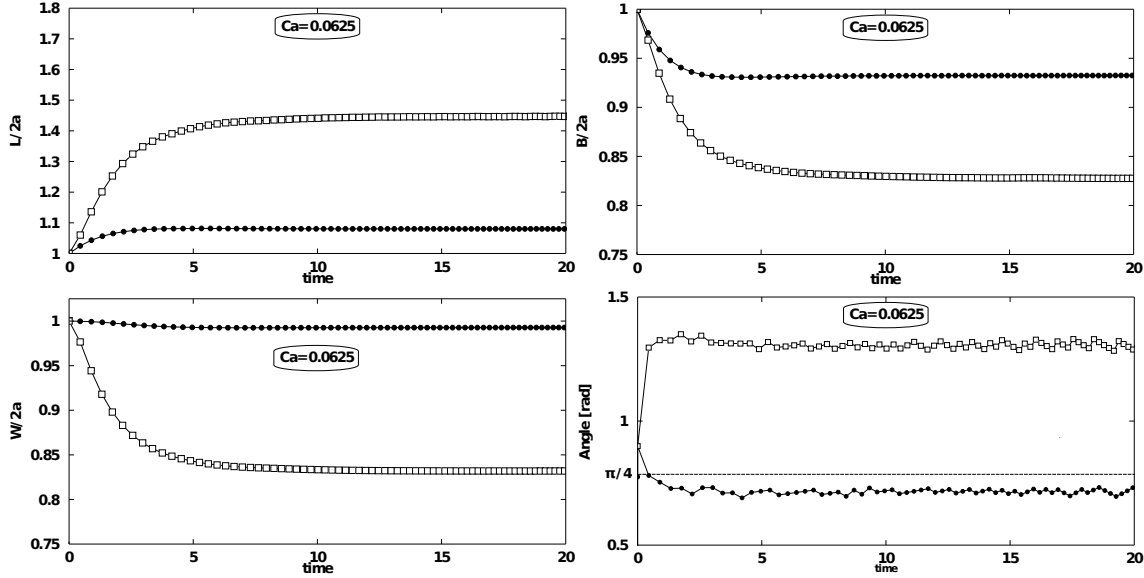


Figure 9: Time evolution of the (scaled) length of the droplet principal axes and the orientation angle for $Ca = 0.0625$ and $Re = 0.2745$. The black circles correspond to the zero external field case ($Bo_m = 0$) and the unfilled squares to $Bo_m = 4.4475$.

to just three values of Bo_m , it is clear that the droplet distortion is nonlinear in Bo_m . Moreover, there is little difference between the droplet deformation for the two smallest values of Bo_m , which indicates that the corresponding droplet distortion is predominantly due to the flow strain. But for $Bo_m = 6.25$, there is a dramatic change in the droplet deformation. The relative variation of L is now more than four times that obtained at the two smaller magnetic Bond numbers. Furthermore, the relative change of W is almost 40% and as large as that of B . In the absence of the applied field, W only experiences a relative change of about 3%. The field-induced distortion of the droplet in the vorticity direction is remarkably large and underlines, again, the three-dimensional character of the problem.

Finally, the last column of Table 3 shows that as Bo_m increases the angle θ of the direction of maximal deformation also increases. This is consistent with the field-induced distortion becoming more and more predominant over the flow strain deformation.

5 Conclusion

We reported on fully three-dimensional numerical simulations of the dynamics and deformation of a sheared ferrofluid droplet immersed in a Newtonian viscous fluid and with applied magnetic field. To our knowledge, this is the first such three-dimensional study.

Bo_m	$100\left(\frac{L-2a}{2a}\right)$	$100\left(\frac{B-2a}{2a}\right)$	$100\left(\frac{W-2a}{2a}\right)$	D	θ [rad]
6.25×10^{-2}	+18.61%	-13.09%	-3.200%	1.543×10^{-1}	0.65
6.25×10^{-1}	+21.40%	-13.19%	-5.425%	1.661×10^{-1}	0.75
$6.25 \times 10^{+0}$	+89.01%	-29.47%	-29.39%	4.565×10^{-1}	1.05

Table 3: Relative changes of the length of the droplet principal axes, Taylor’s deformation parameter D , and the orientation angle θ at steady state for fixed $Ca = 0.125$, $Re = 0.549$.

The consideration of the magnetic effects and solution of the potential equation has increased the computational cost by about 11 %, if considered a time step without Lagrangian mesh optimization. In the context of the reported simulation, the time spent for one optimization is about 30 % greater than a time step without optimization, with the number of optimizations strongly depends on how and how much the interface deforms.

While we consider only a limited number of values of the capillary and the magnetic Bond number, due to the enormous computational cost of each high resolution simulation to steady state, our study shows clearly the significant field-induced distortions of the sheared ferrofluid droplet and the effect of the field on the direction of maximal deformation and on the overall dynamics towards steady state. In particular, we found that for $Bo_m \approx O(1)$ and small Ca (weak flows), the droplet deformation in the vorticity direction can be of the same order as that occurring in the shear plane. This and other results in this study highlight the relevance of the three-dimensional character of this important rheological problem.

The authors gratefully acknowledge financial support by the Brazilian National Council for Scientific and Technological Development CNPq by the Grant # 143471/2011-2 (W.C.J.), the program Ciências Sem Fronteiras Grant # 205962/2014-9 (W.C.J., H.D.C.), CNPq research Grants # 309433/2011-8 and 303514/2014-0 (A.M.R.), and the National Science Foundation Grant DMS 1317684 (H.D.C.). W.C.J. wishes to acknowledge the hospitality of the department of mathematics of University of California, Santa Barbara during his visit in which part of this research was conducted. HDC would like to acknowledge the hospitality of the Vortex Group at the University of Brasilia during his visit in which part of this research was conducted. The authors also thank Profs. Taygoara de Oliveira and Francisco R. Cunha for insightful discussions and suggestions.

A Discretization of the magnetic potential equation and computation of the magnetic force

We discretize equation (2.6) as

$$\mathbf{D} \cdot [\mu \mathbf{G} \psi_{i,j,k}] = 0,$$

where $\mathbf{G} \doteq (D_{\Delta_x}, D_{\Delta_y}, D_{\Delta_z})$ and $\mathbf{D} \doteq (D_{\Delta_x}(\cdot)_x + D_{\Delta_y}(\cdot)_y + D_{\Delta_z}(\cdot)_z)$ are the standard, centered difference approximations of the gradient and the divergence operators, respectively. In the x direction we have

$$D_{\Delta_x}(\psi)_{i,j,k} = \frac{\psi_{i,j,k} - \psi_{i-1,j,k}}{\Delta_x},$$

$$D_{\Delta_x}((\mu \mathbf{G} \psi)_x)_{i,j,k} = \frac{\mu_{i-1/2,j,k} D_{\Delta_x}(\psi)_{i,j,k} - \mu_{i-3/2,j,k} D_{\Delta_x}(\psi)_{i-1,j,k}}{\Delta_x},$$

where $\psi_{i,j,k}$ and $\mu_{i,j,k}$ are the approximations corresponding to the values at the cell centers and $\mu_{i-1/2,j,k} = (1/2)(\mu_{i-1,j,k} + \mu_{i,j,k})$ is the value of μ at the cell face. The discretization in the other directions is performed similarly. This second order finite difference discretization of (2.6) is defined on composite AMR grid. Applying the boundary conditions (of Neumann type in at top and bottom walls and periodic in the other directions), the resulting system of equations is solved using a multilevel multigrid method, similar to that employed for the pressure equation in the projection step of the fluid solver and described in [19]. The method uses a V-cycle recursive form and Gauss-Seidel as a relaxation, using the relaxation to downwards, on the coarsest multigrid level, and to upwards, in a number of 3, 10 and 10 times, respectively. Taking, approximately, 5 iterations to achieve a residual less than 1×10^{-9} .

Once the magnetic potential ψ is obtained, at every time step, the magnetic stress tensor τ_m is approximated to second order using finite differences. The xy component of τ_m is computed *at the cell center* as

$$((\tau_m)_{xy})_{i,j,k} = \tilde{\mu}_{i,j,k} \left(\frac{\psi_{i+1,j,k} - \psi_{i-1,j,k}}{2\Delta_x} \right) \left(\frac{\psi_{i,j+1,k} - \psi_{i,j-1,k}}{2\Delta_y} \right),$$

where $\tilde{\mu}_{i,j,k} = (\mu_{i+1,j,k} + \mu_{i-1,j,k} + \mu_{i,j+1,k} + \mu_{i,j-1,k}) / 4$ is an approximation to μ at the cell edge. The xy component of τ_m *at the cell edge* is computed as the average of the corresponding four closest cell center values. The x component of $\nabla \cdot \tau_m$ is approximated by

$$\begin{aligned} (\nabla \cdot \tau_m)_{xijk} &= \left(\frac{((\tau_m)_{xx})_{i,j,k} - ((\tau_m)_{xx})_{i-1,j,k}}{\Delta_x} \right) \\ &+ \left(\frac{((\tau_m)_{xy})_{i-1/2,j+1/2,k} - ((\tau_m)_{xy})_{i-1/2,j-1/2,k}}{\Delta_y} \right) \\ &+ \left(\frac{((\tau_m)_{xz})_{i-1/2,j,k+1/2} - ((\tau_m)_{xz})_{i-1/2,j,k-1/2}}{\Delta_z} \right), \end{aligned}$$

The other components of τ_m and of $\nabla \cdot \tau_m$ are computed similarly.

The second order accuracy of the scheme to compute ψ , τ_m , and $\nabla \cdot \tau_m$ was verified by the method of manufactured solutions. That is, starting with an arbitrary smooth

function ψ_e , which satisfy the boundary conditions, an exact solution is constructed by modifying the right hand side of (2.6). This exact solution is then used to obtain precise convergence rates of the numerical approximation on a fixed AMR grid.

B Verification of the numerical accuracy

In the absence of any ferromagnetic components ($\tau_m = 0$), (2.1)-(2.2) reduce to the familiar Navier-Stokes equations for an incompressible flow. In that case, the numerical scheme is tested for its accuracy and stability properties, the results being reported in detail by Pivelo (2012) [37] and by Pivelo et al. (2014) [20] who employ the *manufactured solution* strategy to that end. Furthermore, [37] reports also on the accuracy of Lagrangian mesh operations found in the immersed boundary methodology employed here such as the interpolation of Eulerian velocities, the spreading of tension forces, and the interface evolution in time, while Jesus et al. (2015) [19] reports on the Lagrangian mesh optimization and its computational costs along with other comments on efficiency (see also the supplementary material accompanying that later work). In summary, the fluid solver exhibits second-order for the velocity and between first- and second-order accuracy for the pressure. When Lagrangian mesh operations are taken into account, we obtain between first- and second-order accuracy for the entire scheme, the usual accuracy expected in the context of immersed boundary methodologies [21]. To complete the accuracy verification, we consider next the computation of the magnetic force when there is a ferromagnetic component present ($\tau_m \neq 0$).

In the context of the manufactured solution strategy, we select smooth functions to play the role of both the magnetic permeability function, μ , and the (exact) magnetic scalar potential, ψ_e . We test the numerical scheme for computing the magnetic force (2.9) by first solving the elliptic equation for ψ

$$\nabla \cdot (\mu \nabla \psi) = f_e \doteq \nabla \cdot (\mu \nabla \psi_e), \quad (\text{B.1})$$

and then by computing the magnetic tensor as

$$\boldsymbol{\tau}_m = \mu (\mathbf{H} \otimes \mathbf{H}), \quad (\text{B.2})$$

where $\mathbf{H} = \nabla \psi$. The magnetic force is computed by $\mathbf{f}_m = \nabla \cdot \boldsymbol{\tau}_m$. In this context, we note that the right hand side of (B.1) does not vanish in general since we usually select the magnetic scalar potential rather arbitrarily (it does not have to necessarily bear any physical meaning). In real a physical problem, we solve a Laplace equation and not a Poisson equation ($f_e = 0$). For the tests that follow, we choose

$$\psi_e(\mathbf{x}) = \sin\left(\frac{2\pi x}{b_1 - a_1}\right) + \cos\left(\frac{2\pi y}{a_2 - b_2}\right) - a_3 b_3 z + \frac{a_3 z^2}{2} + \frac{b_3 z^2}{2} - \frac{z^3}{3}, \quad (\text{B.3})$$

and as the given magnetic permeability

$$\mu(\mathbf{x}) = \sin^2\left(\frac{2\pi x}{b_1 - a_1}\right) \sin^2\left(\frac{2\pi y}{b_2 - a_2}\right) \sin^2\left(\frac{2\pi z}{b_3 - a_3}\right) + 1, \quad (\text{B.4})$$

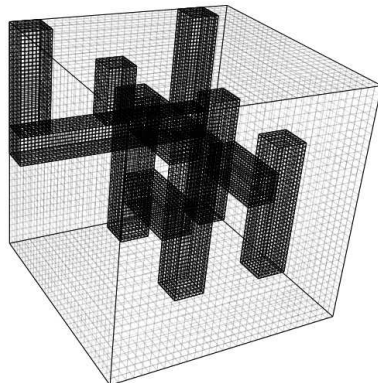


Figure 10: Composite grid employed in the verification of the accuracy in the computation of the magnetic scalar potential and of the magnetic force.

k -th run	k -th c-grid	$E_k = \ \psi - \psi_e\ _2$	$q = \log_2(E_k/E_{k+1})$
$k=1$	$032 \times 032 \times 032\text{L2}$	3.02×10^{-3}	—
$k=2$	$064 \times 064 \times 064\text{L2}$	7.54×10^{-4}	2.0
$k=3$	$128 \times 128 \times 128\text{L2}$	1.88×10^{-4}	2.0
$k=4$	$256 \times 256 \times 256\text{L2}$	4.71×10^{-5}	2.0

Table 4: L2-norm of the error E_k and estimated order of convergence q obtained under grid refinement for the magnetic scalar potential on a two-level composite grid.

where $\mathbf{x} = (x, y, z) \in [a_1, b_1] \times [a_2, b_2] \times [a_3, b_3] = [-0.16, 0.16] \times [-0.16, 0.16] \times [-0.16, 0.16]$. We highlight the fact that by selecting (B.3)-(B.4), we automatically select the exact $\mathbf{H}_e = \nabla \psi_e$ and $\boldsymbol{\tau}_{m_e} = \mu(\mathbf{H}_e \otimes \mathbf{H}_e)$. Of course, the exact magnetic force is also known, $\mathbf{f}_{m_e} = \nabla \cdot \boldsymbol{\tau}_{m_e}$. The idea now is to compare \mathbf{f}_{m_e} with the magnetic force numerically computed from the given magnetic permeability (B.4) and from the numerical solution of (B.1)-(B.2) for which boundary conditions are provided by (B.3) (periodic in x and y directions, and Neumann boundary condition in the z direction).

A study of the convergence under grid refinement is performed for several discretizations of the computational domain. In particular, Tables 4 and 5 present the results on a series composite grids (c-grids) with two levels $n \times n \times n\text{L2}$ which are based on the c-grid displayed in Figure 10, where n is the number of cells in each direction in the first level (base level) and “L2” refers to the total number of grid levels used. Close to second-order convergence behavior is verified for both the magnetic scalar potential and for the magnetic force.

$\ (\nabla \cdot \boldsymbol{\tau}_m)_x - (\mathbf{f}_{m_e})_x\ _2$	q	$\ (\nabla \cdot \boldsymbol{\tau}_m)_y - (\mathbf{f}_{m_e})_y\ _2$	q	$\ (\nabla \cdot \boldsymbol{\tau}_m)_z - (\mathbf{f}_{m_e})_z\ _2$	q
$1.37 \times 10^{+2}$	—	$2.01 \times 10^{+2}$	—	$1.43 \times 10^{+1}$	—
$3.80 \times 10^{+1}$	1.9	$5.12 \times 10^{+1}$	2.0	$3.70 \times 10^{+0}$	2.0
$1.12 \times 10^{+1}$	1.8	$1.40 \times 10^{+1}$	1.9	9.40×10^{-1}	2.0
$3.50 \times 10^{+0}$	1.7	$4.09 \times 10^{+0}$	1.8	2.36×10^{-1}	2.0

Table 5: L2-norm of the error and estimated order of convergence for each component of the magnetic force ($\nabla \cdot \boldsymbol{\tau}_m$ is computed numerically while $\mathbf{f}_{m_e} = \nabla \cdot \boldsymbol{\tau}_{m_e}$ is computed exactly, their components $(\mathbf{f}_{m_e})_x$, $(\mathbf{f}_{m_e})_y$ and $(\mathbf{f}_{m_e})_z$ have magnitudes around $O(10^4)$, $O(10^4)$ and $O(10^3)$, respectively).

Domain Size (2C)	$100 \left(\frac{L-2a}{2a} \right)$	$100 \left(\frac{B-2a}{2a} \right)$	$100 \left(\frac{W-2a}{2a} \right)$	θ [rad]
$05a$	+59.63%	-24.16%	+16.49%	0.99
$10a$	+62.39%	-22.68%	-22.06%	1.03
$20a$	+63.27%	-23.02%	-22.12%	1.03
$40a$	+63.31%	-23.08%	-22.14%	1.03
$80a$	+63.49%	-23.08%	-22.27%	1.03

Table 6: Relative changes of the length of droplet principal axes and the orientation angle θ at steady state for $Bo_m = 4.4475$, $Ca = 0.125$, $Re = 0.549$, $\lambda = 1.5$, $\chi = 0.8903$.

C Influence of the domain size and resolution study

To examine domain size effects on the deformation of the sheared ferrofluid droplet under the influence of a uniform applied magnetic field \mathbf{H}_0 in the normal wall (y) direction, we perform steady state simulations on the computational domain $[-C, C] \times [-C, C] \times [-C, C]$ for C approximately equal to $2.5a$, $5a$, $10a$, $20a$, and $40a$ (these computational domains are labeled $C2.5a$, $C05a$, $C10a$, $C20a$, and $C40a$, respectively). The number of adaptive refinement levels is adjusted so that the finest level is the same in all cases ($h = \Delta_x = \Delta_y = \Delta_z = 0.0775a$). A cross section of the domain with the initial composite grid is shown in Figure 11.

We take $Bo_m = 4.4475$, $Ca = 0.125$, $Re = 0.549$, $\lambda = 1.5$, $\chi = 0.8903$. These dimensionless groups correspond to the case of maximal deformation in our study. As documented in Table 6, the difference between the results corresponding to the domain sizes $40a$ and $80a$ are less than 0.14%. Therefore, to reduce the computational cost we select the computational domain to be of size $40a$.

We also performed a resolution study for the same case of shear droplet deformation ($Bo_m = 4.4475$, $Ca = 0.125$) using three different spatial resolutions: the initial spherical

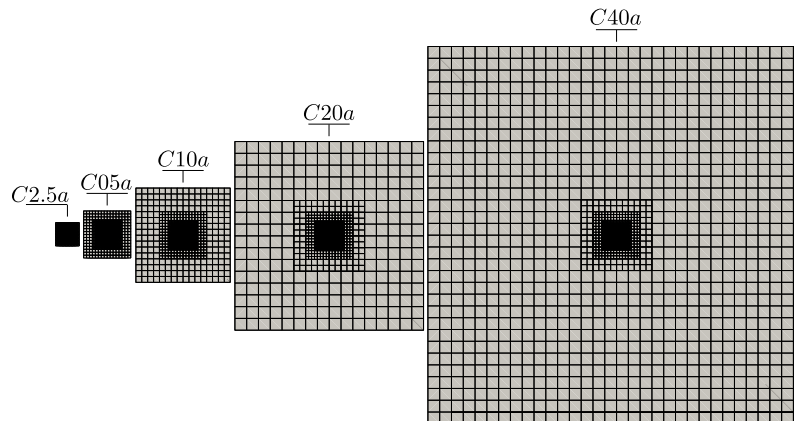


Figure 11: Shear plane cross section of the computational domain and the composite adaptive grid.

droplet was discretized with a Lagrangian mesh of 5120, 20480, and 81920 triangles and the corresponding Eulerian grid resolution was adjusted so that the ratio between the Eulerian and the Lagrangian grid size was approximately 2, which is a common choice for the Immersed Boundary Method [20,21,38].

Figure 12 shows the time evolution of length of the droplet principal axes and Taylor's deformation parameter for the three resolutions. The difference between the results of the two highest resolutions is less than 0.3%. Given this negligible variation in the results and to keep the computational cost affordable, we choose the intermediate resolution for all the numerical studies in this work. Finally, we note that the selected resolution corresponds to a ratio $a/h = 12.91$, where h is the Eulerian grid size inside and around the droplet (finest level of the AMR mesh). Some works of related simulations for two-dimensional or axisymmetric droplets [9,10,14] report that an appropriate a/h should be between 12 and 20.

References

- [1] R. E. Rosensweig, Ferrohydrodynamics, Courier Dover Publications, 1997.
- [2] R. Massart, Preparation of aqueous magnetic liquids in alkaline and acidic media, IEEE Transactions on Magnetics 17 (2) (1981) 1247–1248. doi:10.1109/TMAG.1981.1061188.
- [3] R. Massart, E. Dubois, V. Cabuil, E. Hasmonay, Preparation and properties of monodisperse magnetic fluids, Journal of Magnetism and Magnetic Materials 149 (1) (1995) 1 – 5. doi:http://dx.doi.org/10.1016/0304-8853(95)00316-9. URL <http://www.sciencedirect.com/science/article/pii/0304885395003169>
- [4] O. T. Mefford, R. C. Woodward, J. D. Goff, T. P. Vadala, T. G. S. Pierre, J. P. Dailley, J. S. Riffle, Field-induced motion of ferrofluids through immiscible viscous media: Testbed for restorative treatment of retinal detachment, Journal of Magnetism and

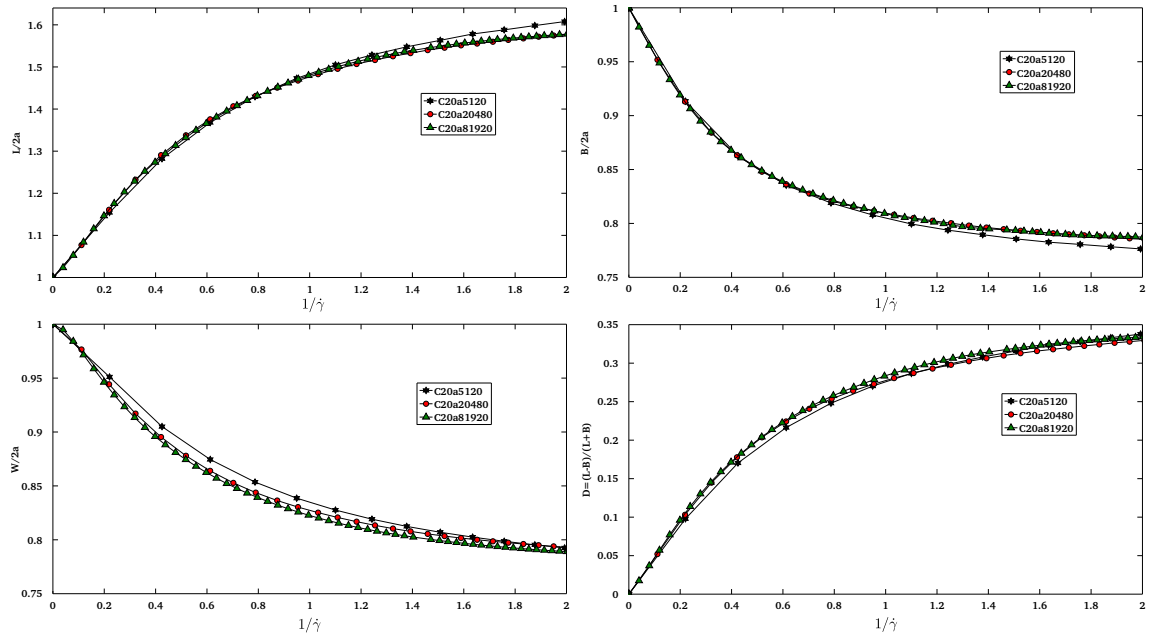


Figure 12: Time (in units of $1/\dot{\gamma}$) evolution of the length of the droplet principal axes and Taylor's deformation parameter D for the numerical resolutions given by 5120 (C20a5120), 20480 (C20a20480) and 81920 (C20a81920) triangles on the droplet surface and with a corresponding Eulerian grid of size approximately twice that of the Lagrangian triangulation. $Bo_m = 4.4475$, $Ca = 0.125$, $Re = 0.549$, $\lambda = 1.5$, $\chi = 0.8903$.

- Magnetic Materials 311 (1) (2007) 347 – 353, proceedings of the Sixth International Conference on the Scientific and Clinical Applications of Magnetic Carriers SCAMC-06. doi:<https://doi.org/10.1016/j.jmmm.2006.10.1174>.
URL <http://www.sciencedirect.com/science/article/pii/S0304885306025728>
- [5] C. Alexiou, R. Schmid, R. Jurgons, C. Bergemann, W. Arnold, F. G. Parak, Targeted Tumor Therapy with “Magnetic Drug Targeting”: Therapeutic Efficacy of Ferrofluid Bound Mitoxantrone, Springer Berlin Heidelberg, Berlin, Heidelberg, 2002, pp. 233–251.
URL https://doi.org/10.1007/3-540-45646-5_12
- [6] P. Voltairas, D. Fotiadis, L. Michalis, Hydrodynamics of magnetic drug targeting, Journal of Biomechanics 35 (6) (2002) 813 – 821. doi:[http://dx.doi.org/10.1016/S0021-9290\(02\)00034-9](http://dx.doi.org/10.1016/S0021-9290(02)00034-9).
URL <http://www.sciencedirect.com/science/article/pii/S0021929002000349>
- [7] P. Yue, S. Lee, S. Afkhami, Y. Renardy, On the motion of superparamagnetic particles in magnetic drug targeting, Acta Mechanica 223 (3) (2012) 505–527. doi:10.1007/s00707-011-0577-9.
URL <http://dx.doi.org/10.1007/s00707-011-0577-9>
- [8] A. S. Lübke, C. Alexiou, C. Bergemann, Clinical applications of magnetic drug targeting, Journal of Surgical Research 95 (2) (2001) 200 – 206. doi:<http://dx.doi.org/10.1006/jsre.2000.6030>.
URL <http://www.sciencedirect.com/science/article/pii/S002248040096030X>
- [9] D. Shi, Q. Bi, R. Zhou, Numerical simulation of a falling ferrofluid droplet in a uniform magnetic field by the voset method, Numerical Heat Transfer, Part A: Applications 66 (2) (2014) 144–164. arXiv:<http://dx.doi.org/10.1080/10407782.2013.869459>, doi:10.1080/10407782.2013.869459.
URL <http://dx.doi.org/10.1080/10407782.2013.869459>
- [10] S. Afkhami, Y. Renardy, M. Renardy, J. S. Riffle, T. St Pierre, Field-induced motion of ferrofluid droplets through immiscible viscous media, Journal of Fluid Mechanics 610 (2008) 363–380. doi:10.1017/S0022112008002589.
- [11] O. Lavrova, G. Matthies, V. Polevikov, L. Tobiska, Numerical modeling of the equilibrium shapes of a ferrofluid drop in an external magnetic field, PAMM 4 (1) (2004) 704–705. doi:10.1002/pamm.200410333.
URL <http://dx.doi.org/10.1002/pamm.200410333>
- [12] O. Lavrova, G. Matthies, T. Mitkova, V. Polevikov, L. Tobiska, Numerical treatment of free surface problems in ferrohydrodynamics, Journal of Physics: Condensed Matter 18 (38) (2006) S2657.
URL <http://stacks.iop.org/0953-8984/18/i=38/a=S09>
- [13] M. Korlie, A. Mukherjee, B. Nita, J. Stevens, A. Trubatch, P. Yecko, Modeling bubbles and droplets in magnetic fluids, Journal of Physics: Condensed Matter 20 (20) (2008) 204143.
- [14] S. Afkhami, A. J. Tyler, Y. Renardy, M. Renardy, T. G. St. Pierre, R. C. Woodward, J. S. Riffle, Deformation of a hydrophobic ferrofluid droplet suspended in a viscous medium under uniform magnetic fields, Journal of Fluid Mechanics 663 (2010) 358–384. doi:10.1017/S0022112010003551.
- [15] G.-P. Zhu, N.-T. Nguyen, R. V. Ramanujan, X.-Y. Huang, Nonlinear deformation of a ferrofluid droplet in a uniform magnetic field, Langmuir 27 (24) (2011) 14834–14841, pMID: 22044246. arXiv:<http://dx.doi.org/10.1021/la203931q>, doi:10.1021/la203931q.
URL <http://dx.doi.org/10.1021/la203931q>
- [16] V. G. Bashtovoi, O. A. Lavrova, V. K. Polevikov, L. Tobiska, Computer modeling of the instability of a horizontal magnetic-fluid layer in a uniform magnetic field, Journal of Magnetism

- and Magnetic Materials 252 (2002) 299 – 301, proceedings of the 9th International Conference on Magnetic Fluids. doi:[https://doi.org/10.1016/S0304-8853\(02\)00598-X](https://doi.org/10.1016/S0304-8853(02)00598-X).
URL <http://www.sciencedirect.com/science/article/pii/S030488530200598X>
- [17] G. Matthies, L. Tobiska, Numerical simulation of normal-field instability in the static and dynamic case, *Journal of Magnetism and Magnetic Materials* 289 (2005) 346 – 349, proceedings of the 10th International Conference on Magnetic Fluids. doi:<https://doi.org/10.1016/j.jmmm.2004.11.098>.
URL <http://www.sciencedirect.com/science/article/pii/S030488530401323X>
- [18] H. Knieling, R. Richter, I. Rehberg, G. Matthies, A. Lange, Growth of surface undulations at the rosenzweig instability, *Phys. Rev. E* 76 (2007) 066301. doi:10.1103/PhysRevE.76.066301.
URL <http://link.aps.org/doi/10.1103/PhysRevE.76.066301>
- [19] W. C. D. Jesus, A. M. Roma, M. R. Pivello, M. M. Villar, A. D. Silveira-Neto, A 3d front-tracking approach for simulation of a two-phase fluid with insoluble surfactant, *Journal of Computational Physics* 281 (2015) 403 – 420. doi:<https://doi.org/10.1016/j.jcp.2014.10.021>.
URL <http://www.sciencedirect.com/science/article/pii/S0021999114007037>
- [20] M. R. Pivello, M. M. Villar, R. Serfaty, A. M. Roma, A. Silveira-Neto, A fully adaptive front tracking method for the simulation of two phase flows, *International Journal of Multiphase Flow* 58 (2014) 72 – 82. doi:<https://doi.org/10.1016/j.ijmultiphaseflow.2013.08.009>.
URL <http://www.sciencedirect.com/science/article/pii/S0301932213001286>
- [21] C. S. Peskin, The immersed boundary method, *Acta Numerica* 11 (2002) 479–517. doi:10.1017/S0962492902000077.
- [22] C. S. Peskin, Numerical analysis of blood flow in the heart, *Journal of Computational Physics* 25 (3) (1977) 220 – 252. doi:[http://dx.doi.org/10.1016/0021-9991\(77\)90100-0](http://dx.doi.org/10.1016/0021-9991(77)90100-0).
URL <http://www.sciencedirect.com/science/article/pii/0021999177901000>
- [23] M. J. Berger, P. Colella, Local adaptive mesh refinement for shock hydrodynamics, *Journal of Computational Physics* 82 (1) (1989) 64 – 84. doi:[http://dx.doi.org/10.1016/0021-9991\(89\)90035-1](http://dx.doi.org/10.1016/0021-9991(89)90035-1).
URL <http://www.sciencedirect.com/science/article/pii/0021999189900351>
- [24] M. Berger, I. Rigoutsos, An algorithm for point clustering and grid generation, *IEEE Transactions on Systems, Man, and Cybernetics* 21 (5) (1991) 1278–1286. doi:10.1109/21.120081.
- [25] H. Edelsbrunner, N. R. Shah, Incremental topological flipping works for regular triangulations, *Algorithmica* 15 (3) (1996) 223–241. doi:10.1007/BF01975867.
URL <http://dx.doi.org/10.1007/BF01975867>
- [26] L. D. Landau, E. M. Lifshitz, *Electrodynamics of Continuous Media*, Vol. 8, Pergamon Press, 1960, (Volume 8 of A Course of Theoretical Physics) Second impression in English 1963.
- [27] J. M. Rallison, The deformation of small viscous drops and bubbles in shear flows, *Annu. Rev. Fluid Mech.* 16 (1984) 45–66.
- [28] H. A. Stone, Dynamics of drop deformation and breakup in viscous fluids, *Annual Review of Fluid Mechanics* 26 (1) (1994) 65–102.
- [29] G. I. Taylor, The viscosity of a fluid containing small drops of another fluid, *Proceedings of the Royal Society of London. Series A, Containing Papers of a Mathematical and Physical Character* 138 (834) (1932) 41–48.
URL <http://www.jstor.org/stable/96007>
- [30] L. G. Leal, *Advanced Transport Phenomena: Fluid Mechanics and Convective Transport Processes*, Cambridge University Press, United States of America by Cambridge University Press, New York, 2007, (Part of Cambridge Series in Chemical Engineering).
- [31] M. Zahn, *Electromagnetic Field Theory: A Problem Solving Approach*, 1st Edition, Malabar,

- FL: Krieger Publishing Company, 2003, (First published 1979 by John Wiley and Sons).
- [32] V. I. Arkhipenko, Y. D. Barkov, V. Bashtovoi, Shape of a drop of magnetized fluid in a homogeneous magnetic field, English translation: *Magnetohydrodynamics* 14 (1978) 131–134.
 - [33] V. I. Drozdova, T. V. Skrobotova, V. V. Chekanov, Experimental study of the hydrostatics characterizing the interphase boundary in a ferrofluid., *Magnetohydrodynamics* New York, N. Y. 15 (1) (1979) 12–14.
URL <http://www.scopus.com/inward/record.url?eid=2-s2.0-0018334608&partnerID=40&md5=c71ff29792d56027c0e67675a8779f9b>
 - [34] F. Greco, Second-order theory for the deformation of a newtonian drop in a stationary flow field, *Phys. Fluids* 14 (2002) 946–954.
 - [35] S. Guido, F. Greco, Dynamics of a liquid drop in a flowing immiscible fluid, *Rheology Reviews* (2004) 99–142.
 - [36] Z. Zapryanov, S. Tabakova, *Dynamics of Bubbles, Drops and Rigid Particles*, Vol. 50, Springer Science & Business Media, 1998.
 - [37] M. R. Pivello, A fully adaptive front tracking method for the simulation of 3d two-phase flows, Ph.D. thesis, Faculdade de Engenharia Mecânica, Universidade Federal de Uberlândia, Brasil (Julho 2012).
 - [38] M.-C. Lai, Y.-H. Tseng, H. Huang, An immersed boundary method for interfacial flows with insoluble surfactant, *Journal of Computational Physics* 227 (15) (2008) 7279 – 7293.
doi:<https://doi.org/10.1016/j.jcp.2008.04.014>.
URL <http://www.sciencedirect.com/science/article/pii/S0021999108002283>